Mechanism of Photoluminescence in Intrinsically Disordered $CaZrO_3$ Crystals: First Principles Modeling of the Excited Electronic States

Marisa Carvalho Oliveira[1,2], Lourdes Gracia[3], Marcelo de Assis[2], Ieda Lúcia Viana Rosa[2], Maria Fernanda do Carmo Gurgel[4], Elson Longo[2], and Juan Andrés*[1]

1 Department of Analytical and Physical Chemistry, University Jaume I (UJI), Castelló E-12071, Spain
2 CDMF-UFSCar, Universidade Federal de São Carlos, PO Box 676, 13565-905 São Carlos, SP, Brazil
3 Department of Physical Chemistry, University of Valencia, Burjassot E-46100, Spain
4 Department of Chemistry, Universidade Federal de Goiás, Regional Catalão, Av.Dr.Lamartine Pinto d eAvelar,75704-020, Catalão, GO, Brazil.

*E-mail: andres@qfa.uji.es

Abstract

$CaZrO_3$ (CZO) powders were synthesized at different temperatures (400, 600, 800, and 1000 °C) and characterized by X-ray diffraction, Raman and ultraviolet-visible spectroscopic methods, along with photoluminescence (PL) emissions. First principle calculations based on the density functional theory (DFT), using a periodic cell models, provide a theoretical framework for understanding the PL spectra based on the localization and characterization of the ground and electronic excited states. Fundamental (singlet, *s*) and excited (singlet, *s**, and triplet, *t**) electronic states were localized and characterized using the ideal and distorted structures of CZO. Their corresponding geometries, electronic structures, and vibrational frequencies were obtained. A relationship between the different morphologies and structural behavior has also been established.

Polarized structures were identified by the redistribution of the $4d_z2$, $4d_{yz}$, and $4d_{xy}$ (Zr) orbitals at the conduction band and the $2p_z$ (O) orbital in the valence band for *s*, *s** and *t**. Analysis of the vibrational eigenvector modes of these electronic states reveals a relationship between them via asymmetric bending and stretching modes that arise from Zr atom displacements due to polyhedral [ZrO_6] distortion. Furthermore, the results provided an insight into the PL emissions of the as-synthesized $CaZrO_3$ and led to the conclusion that the presence of electronically excited states is strongly related to the structural order-disorder effects (polyhedral distortion) at short range for both [ZrO_6] and [CaO_8] clusters.

1. Introduction

The importance of the local structure in determining the observable properties of a material has been discussed since the advent of crystallography [1]. Therefore, the physical and chemical properties of ceramics are intimately linked to their local structure, characterized by the regular and repeating geometry associated with the primitive lattice. While the concept of a crystalline solid as a perfect, periodic structure is at the core of our understanding of a wide range of material properties, disorder is in reality ubiquitous, and can influence various properties drastically. In typical ferroelectric crystals, the polarization and related properties result from structural lattice distortions. For example, in $BaTiO_3$, the off-centering displacement of Ti in the $[TiO_6]$ octahedron is the origin of its exceptional dielectric properties [2]. Very recently, different possibilities to explain the PL emissions in crystalline $Ba(Zr_xTi_{1-x})O_3$ were associated to the isomorphic Zr/Ti substitutions and structural distortions at the $[ZrO_6]$ octahedra [3].

According to the electronic band theory, band formation requires a periodic potential, typically established by regularly spaced atoms in a crystal lattice. When this periodicity is perturbed—for example, when electromagnetic radiation interacts with matter—the structural and electronic order-disorder effects appear, inducing the presence of intermediate states within the band gap, as well as enhancing the anisotropy of the chemical bonds in the materials. These effects are concomitant with the presence of excited electronic states from the ground state after the activation process, determining to a larger extent the efficiency and the spectral features of emitted radiation. Following the classical paper of Blasse [4], the luminescence of self-activated closed-shell transition metal oxides is basically of charge transfer character.

In this context, PL emission is well suited for the characterization of crystalline materials based on broad band gap semiconductors. In particular, our group is involved in a research project on binary and complex metal oxides as potential alternatives to traditional metal activator based phosphors, because of their advantages of low toxicity, stability, tunable emission color, and low cost. These oxides include TiO_2 [5], ZnO [6], ZnS [7], SnO_2 [8], molybdates [9-11], and tungstates [12, 13]. Among the numerous types of perovskite materials (ABO_3), alkaline earth metal perovskite oxides are a

veritable gold mine of diverse physical and chemical properties with large technological applications [14-21] based on ferroelectricity, piezoelectricity, non-linear optical behavior, and PL emissions, that that arise from the absence of inversion symmetry in a crystal structure [22]. ABO_3 perovskite compounds have a large cation at the A-site, a smaller cation at the B-site, and the oxygen O acts as a bridging ligand, linking the B-site cations to form a three-dimensional cage-like host framework consisting of anionic $[BO_3]^-$ cages enclosed by 12 B–O-B fragments and filled by A-site guest cations. The ideal structure of perovskite oxides has the cubic space group Pm3m, and the structural variations from the ideal cubic prototype mainly arise from the displacement of the A- and B-site cations and the tilting of the $[BO_6]$ octahedra, based on Glazer's exhaustive classification of the tilted octahedral [23, 24].

Symmetry-breaking processes have long played a central role in the design of functional materials. An important example is the rich PL behavior in the ABO_3 perovskite oxides which originate, at least in part, from the structural and electronic order-disorder effects of the $[BO_6]$ octahedra through distortions and rotations. Octahedral rotations provoke changes in the B-O and A-O bond lengths as well as B-O-B and A-O-A bond angles, shifting the positions of the oxygen ions from the edges of the cubic perovskite structure [25]. The overall result is that the unit cell deforms and the structure is no longer cubic but of reduced symmetry, such as orthorhombic, rhombohedral, tetragonal, monoclinic, and triclinic phases, depending on the details of the $[BO_6]$ octahedral rotations and B-site distortions. This influences the electronic and optical properties of materials, behavior of photo-generated charge carriers, including excitation, transfer, and redox reactions, and plays an important role in their technological applications [6, 17, 26-30]. It should be realised that the absorption transition of the $[BO_6]$ cluster corresponds to an electron transition from a bonding to a nonbonding molecular orbital, i.e. the chemical bond is perturbed, so that the $[BO_6]$ cluster is distorted.

The disorder is considered intrinsic if it is associated with the localization of electrons and electron holes, provoking the presence of different electronic states within the band gap. These electronic states are responsible for the PL behavior. The excitation induced by electromagnetic radiation promotes electrons from the valence band (VB) to the conduction band (CB) by this process. These phenomena originate from the interactions between matter and external incoming light, and an electronic excited state is obtained when a system (crystal) is in an energy level higher than the ground state,

e.g., after the absorption of one or more quanta of light (photons). The structure and charge distribution of both fundamental and electronic excited and short-lived states are key to understanding the optical properties. It is necessary to emphasize that PL emissions are microscopic in origin and the structures of these short-lived excited states are difficult to obtain. Excited electronic states reveal information about the electronic structures of the material, but they are short-lived and highly reactive, making the quest to manipulate them extremely demanding.

The difficulties encountered in separating complex factors during experiments are not present when employing theoretical models based on quantum mechanics, which is a reliable tool to describe these systems at the microscopic scale. Consequently, one has to resort to quantum chemical simulations to provide a better understanding of experiments in order to help in ascertaining the geometry and electronic structure of the electronic excited states and therefore prediction, of the PL behavior. However, modeling the structure of excited electronic states and their properties using the first-principles electronic structure methods is still a huge challenge. To overcome this difficulty, numerous efforts by our research group have been made to understand the mechanism of PL emissions in $SrTiO_3$, $SrTiO_3$:Sm, $CaWO_4$, $BaZrO_3$, and $BaZr_{1-x}Hf_xO_3$ solid solutions based on the characterization of excited electronic states [31-37], where the computational cost is significantly reduced by imposing periodic boundary conditions.

Calcium zirconate, $CaZrO_3$ (CZO), has received a lot of attention due to its exceptional dielectric and catalytic properties and PL emissions with applications in diverse areas of science and technology such as hydrogen sensors, luminescence hosts, multilayer capacitors, catalysis, and so on [38-48] CZO presents an orthorhombic structure with 8 and 6-coordination for the Ca and Zr atoms, [CaO_8] and [ZrO_6], respectively, as the constituent building blocks of this material [49]. There are several reports on the electronic structure calculations performed to study CZO in the ground state [50-55]. Recently, Gupta et al. [56] have been performed a spectroscopic and theoretical study to explain the PL emission in the blue region based on the nature of defects, while Moreira et al. [57] employed first-principles calculations to clarify the mechanisms involved in the luminescence emissions observed for disordered $BaZrO_3$, proposing a novel explanation for transitions from a PL and to a radioluminescence emission regime based on crystalline defects.

Nevertheless, no insights about the PL emissions based on the presence of electronic excited states have been obtained. The focus of this article is to expand the theoretical understanding of the phenomena in CZO as a result of an analysis of the electronic excited states. First principles calculations are employed in the present research, and we argue that because our procedure generates models in accord to the experiment, our methodological approach is valid. In addition, a careful examination of the calculated results provides an insight into the physical origin of the process that accounts for the PL behavior of CZO materials. Full details, describing the generation of the atomistic models are presented in the Supplementary Information.

In the present work the focus is the PL mechanism and its relationship with the presence of excited electronic states in intrinsically disordered $CaZrO_3$ crystals, and we seek to fulfill a three-fold objective: synthesis and characterization by X-ray diffraction (XRD), Raman and UV-Vis spectroscopy, and PL emissions of the as-synthesized CZO samples; employment of first principles calculations based on the density functional theory (DFT), at B3LYP level, to localize and characterize (geometry, electronic properties, and vibration frequencies) both ground and excited electronic states of CZO (electronic structures, including density of state (DOS) and band structures were calculated based on optimized geometries); and the achievement of a relationship between structural and electronic order-disorder effects and PL emissions.

The remainder of the paper is organized as follows; the analysis and discussion of both theoretical and PL results are presented in Section 3. The main conclusions are given in Section 4.

2. Experimental procedures and computational details

2.1. Synthesis and characterization

The powder CZO was prepared by the method of polymeric precursor, kept for 4 hours at 400 °C to remove any carbon, which is taken to a further heat treatment up to 1000 °C for 2h [58].

The synthesized samples at 400, 600, 800 and 1000°C were characterized by XRD (Rigaku DMax2500PC) using Cu KR (λ) 1.5406 Å radiation. The data were collected from 10° to 120° in the 2θ range with 0.5° divergence slit, 0.3 mm receiving slit, in fixed-time mode with 0.02° step size and Is/point. Crystal structures were

identified and refined by the Rietveld method using the GSAS software [59]. This software is specially designed to refine simultaneously both the structural and the microstructural parameters through a least squares method. The peak profile function was modeled using the convolution of the Thompson-Cox-Hastings pseudo-Voigt (pV-TCH) with the asymmetry function described by *Finger et. al*. [60]. The Rietveld refinement is presented in a previous reported study [61], and provides the network parameters a, b, and c as well as internal coordinates, space group of the CZO and refinement of quality indicators.

PL spectra we are measured with an Ash Monospec 27 monochromator (Thermal Jarrel, U.S.A.) and a R4446 photomultiplier (Hamamatsu Photonics, U.S.A.). The 350 nm excitation wavelength of a krypton ion laser (Coherent Innova 90 K) was used as excitation source, keeping its maximum output power at 200 mW.

Synthesis were performed at different temperatures at 400, 600, 800 and 1000 °C and Raman, PL, XRD spectra were measured at room temperature.

2.2. Computational details

Theoretical calculations were performed using the periodic quantum mechanical method implemented with the computer program CRYSTAL14 [62]. The computational method used is based on density functional theory (DFT) together with the B3LYP functional [63]; [64]. This computational technique has been successful for the study of the electronic and structural properties of various materials including perovskites and several other oxides [36]; [65]. The standards (6-31d1G) all electron basis set were used to describe the atomic orbitals of calcium [66], zirconium [67] and oxygen [68] atoms. The diagonalization of the Fock matrix was performed at 27 or 36 *k*-points grids in the reciprocal space for bulk singlet (s) or excited singlet (s*) and triplet (t*) electronic states, while 9 or 10 *k*-points grids were used for surfaces in singlet (s and s*) or triplet (t*), respectively, of the CZO system. The thresholds controlling the accuracy of the calculation of the Coulomb and exchange integrals were set to 10^{-8} (ITOL1 to ITOL4) and 10^{-14} (ITOL5), and the percent of Fock/Kohn-Sham matrices mixing was set to 40 (IPMIX keyword) [69]. The XCrysDen program was used as a graphical tool to design the spin density plots and VESTA program was used for the design of morphology.

We use periodic models to find the ground and excited electronic states. A 1x1x1 cell was used as a periodic model to represent the fundamental *s* electronic state,

while s* and t* excited electronic states were modeled by shifting the zirconium by a (0.0 0.0 0.2) Å vector from its previous position in the cell **(Fig.1a and b).**

Fig. 1

CZO presents an orthorhombic structure with space group *Pcmn*. An excited state is obtained by imposing a low and high spin state that must promote an electron from the VB to the CB. Per unit cell, this transaction corresponds to imposing two electrons with the opposite (singlet) and same spin (triplet). It also creates a Frenkel exciton (hole in the VB, electron in the CB). To find the excited electronic states, two arrangements have been explored based in the same model but changing the optimization conditions: i) Zr displacement from the center of a [ZrO_6] octahedron in the orthorhombic CZO, followed by an arising of a spontaneous polarization from this asymmetrical structure, resulting in the Jahn–Teller effect [70], fixing the cell parameters to obtain the excited singlet, s*; ii) Zr displacement from the center of a [ZrO_6] octahedron, in which the position of the six nearest oxygen atoms surrounding the Zr atom is optimized as well as cell parameters to find the excited triplet, t*, in which, distorted clusters [CaO_8] are also obtained. Then, a series of calculations were carried out on each different electronic states in order to determine their electronic structures and the specific atomic states which make up their corresponding energies. This information is used to understand the transitions associated with PL emission behavior.

Vibrational analysis for ground and excited electronic states in their equilibrium configurations has been made to ensure that there are no imaginary frequencies corresponding to the saddle points on the potential energy surface. It is well known that DFT calculation at B3LYP method tends to overestimate the values of the vibrational frequencies; therefore, a scaling factor of 0.94 is used [71].

Slab models containing in singlet 8 molecular units (in singlet state) and 4 molecular units (in triplet state) for (121), (100), (010), (101), (001), (111), and (011) surfaces, respectively, were considered, after corresponding energy convergence tests. The surface energy is calculated by using the following equation:

$$E_{suf} = \frac{1}{2A}(E_{slab} - N \cdot E_{bulk})$$

where A is the surface area of each slab, N is the number of molecular units, E_{slab} is the total energy of the slab, E_{bulk} is the total energy per molecular unit for the CZO unit cell. A classic Wulff construction can be obtained, from calculated E_{surf} values, that minimizes the total surface free energy at a fixed volume.

3. Results and Discussion

3.1. X-ray diffraction analysis

CZO crystals were synthesized by the polymeric precursor method and their structural and electronic properties have been studied previously [58]. The X-ray diffraction patterns for the CZO sample at different temperatures are shown in **Fig. 2**, and indicate a single phase orthorhombic perovskite with the *Pcmn* space group. The diffraction peaks were indexed based on the JCPDS 35-0790 file and the crystallization of CZO is observed. In synthesized samples at 400 and 600 °C, the peaks appear more widened and the material is structurally less organized at long range and disordered at short range, involving disordered [CaO_8] and [ZrO_6] clusters, as constituent building blocks of CZO; this behavior can be attributed to structural distortion from the parent high-symmetry structure.

Fig. 2.

3.2. Photoluminescence properties

Fig. 3 displays the PL emission spectrum of the CZO sample synthesized at 1000°C. An emission band extending from 350 to 850 nm and peaking around 450 nm is seen. Additionally, low PL emission intensity was observed at synthesized samples of 400 and 800°C, while at 600°C the PL emission is absent. This indicated that the PL behavior of CZO is sensitive to temperature, and a high PL emission requires a certain amount of order together with disorder in the CZO samples. This is also indicated by the diffraction peaks in **Fig. 3**, which become broader indicating an increase of structural order at short range at both synthesized samples at 800 and 1000°C in the lattice. The PL emissions of perovskite-based materials depend on different aspects, among them the excitation wavelength and synthesis method. In the present work both factors are different of those used in the paper by Gupta et al. [56]. Our results are in line with previous results on different perovskite-based materials [27, 72].

Fig. 3.

3.3. Raman Spectra

The Raman spectra with ten active modes are shown in **Fig. 4**.

CZO with the orthorhombic structure and D^{16}_{2h} (*Pcmn*) symmetry group, presents the following irreducible representations at the Γ point of the Brillouin zone and distribution among the following symmetries:

$$8A_u + 10B_{1u} + 8B_{2u} + 10B_{3u} + 7A_g(R) + 5B_{1g}(R) + 7B_{2g}(R) + 5B_{3g}(R) \quad (1)$$

where $7A_g + 5B_{1g} + 7B_{2g} + 5B_{3g}$ are a total of 24 Raman (R) active modes, $9B_{1u} + 7B_{2u} + 9B_{3u}$ are the 25 infrared active modes, $8A_u$ are non-active modes, along with three translational modes ($B_{1u} + B_{2u} + B_{3u}$) [73, 74].

The Raman spectra with ten active modes are shown in **Fig. 4**. The bands in the range 140–300 cm^{-1} are associated with O-Zr-O torsion modes. The bands at 433 and 464 cm^{-1} are related to the O-Zr-O bending modes and the band at 537 cm^{-1} results from the Zr-O stretching mode. The Raman spectrum of synthesized sample at 900°C was previously reported and compared to other experimental studies [58], showing that this kind of system is typically observed in the low wave number range 145–547 cm^{-1} [73], 143–545 cm^{-1} [75], 153–515 cm^{-1} [76].

The appearance of three vibration modes of synthesized sample at 1000°C, which are not present at temperatures of synthesized samples at 400 and 600°C, was noted. This can be associated with the local distortion of the [ZrO_6] octahedra, causing a breakdown of the Raman selection rules and the presence of weak bands in the Raman spectra. Then, the PL emissions can then be related to the appearance of new vibrational modes at 1000°C.

Fig. 4.

3.4. Theoretical Study

The ground state of CZO has an orthorhombic structure, with both [ZrO_6] and [CaO_8] clusters as the building blocks. To find excited electronic states, different models have been used to achieve a slight distortion in the [ZrO_6] octahedra. The transformation from the fundamental *s* to *s** states occurs following a displacement of 0.2 Å, for 25% of the Zr atoms along the (001) direction. As a result of Zr atom displacement from the center of the [ZrO_6] octahedron, a spontaneous polarization is

produced and a Jahn–Teller effect and asymmetrical relaxation of the six nearest oxygen atoms surrounding the Zr atom in the [ZrO_6] cluster occurs.

However, the transformation from the fundamental *s* to *t** states is produced by a slight distortion of [ZrO_6] and [CaO_8] clusters with a structural order-disorder effect in the Zr-O and Ca-O bonds of CZO. An analysis of the results shows that the transformation from the fundamental *s* to *s** is produced by a slight distortion of [ZrO_6] clusters on a very flat energy surface. For the *t** state an expansion of cell parameters of ~1.5% is found: the *a* parameter increases from 5.594 to 5.673 Å, *b* parameter from 8.021 to 8.155 Å, and *c* parameter from 5.761 to 5.844 Å. In particular, the displacement of the Zr atom causes a slight distortion of both Zr2 and Zr4 clusters, as well as the Ca3 and Ca4 clusters, the latter forming [CaO_{6+2}] clusters. A schematic representation of the unit cells in terms of their cluster constituents is presented in **Fig. 5.** The Ca-O and Zr-O bond distances for the three systems, *s*, *s**, and *t** configurations are listed in **Table 1**.

Table 1.

Fig. 5.

It is important to note that the Zr-O bond distances in the *t** state are stretched and shortened to 2.294 and 1.995 Å, respectively (see **Table 1**), and this effect can be related to the structural order-disorder effect associated with the appearance of PL at 1000 °C.

The characterization of the spin density distribution can be useful for understanding the PL properties of CZO that are based on the behavior of the d-orbitals occupied by unpaired electrons, that is the difference between the contributions from spin alpha and beta to the total electron density. The spin charge density localized in the *t** state is shown in **Fig. 6**, in which Zr2 and O10 are the atoms with the highest spin density. The spin charge density is mainly located in the $4d_{z2}$, $4d_{yz}$, and $4d_{xy}$ orbitals of Zr2 and the O10 $2p_z$ orbital.

Fig. 6.

The results presented in **Fig. 6** and **Table 1** indicate that the triplet state is achieved by a structural distortion. This order-disorder effect may also be noted in the behavior of PL of CZO, which is highly sensitive to temperature. This behavior is due

to the appearance of various electronic levels at this temperature, i.e., intermediate states that are brewing in the band gap. This fact is directly related to the redistribution of local density around Zr and Ca cations that is proportional to the local distortions at both [ZrO_6] and [CaO_8] clusters as well as to torsion movements involving [ZrO_6]-[CaO_8] frameworks. In this way, different types of defects can generate intermediate states and directly influence the band gap.

The PL analysis shows an intracluster organization (short range order), but indicates a disorder between the clusters (medium range order). At medium range the interactions occur by orientation and are associated with the rotation of the dipole moments [ZrO_6]-[ZrO_6], [CaO_8]-[CaO_8] or [ZrO_6]-[CaO_8]. At short range the interactions arise through an induction by permanent dipole moment of the neighboring cluster [CaO_8] or [ZrO_6], i.e. polarization of clusters, and at long range a dispersion from the correlation between electrons in the vicinity of clusters [ZrO_6] or [CaO_8] takes place.

These structural changes are related to theoretical results that have shown that the process of breaking of symmetry (order/disorder) in a structure is a necessary condition for the existence of energy levels in the forbidden band gap. Therefore, for the present, it is considered that within the CZO network, structural distortions emerge between the $[ZrO_6]_o^x - [ZrO_6]_d^x$ and/or $[CaO_8]_o^x - [CaO_8]_d^x$ (o-ordered; d-distorted) clusters that allow transfers electronics between them.

3.4.1 Vibrational analysis

There are 24 Raman-active modes for the orthorhombic structure of CZO according to Equation 1. However, as noted previously (Section 3.3) not all of these bands can be observed experimentally. It is possible that many of the predicted modes are hidden by other intense bands, which may overlap or involve very low changes in the polarizability.

Table 2.

In **Table 2** the theoretical calculated values are presented and compared to experimental data at different temperatures. An analysis of the results shows some discrepancies in a few cases, and to shed light on them a representation of Raman vibration movements above 370 cm^{-1} are depicted in **Fig. 7a**. The A_g mode (at 370.49

cm^{-1}) corresponds to a Zr-O-Ca bending motion between the clusters, whereas higher values at ~480 cm^{-1} are associated with the O-Zr-O bending. A sum of the B_{1g} and A_g modes is obtained experimentally at ~430 cm^{-1} that corresponds to the theoretical modes at 434.82 and 450.96 cm^{-1}, whereas the theoretical B_{3g} mode at 479.59 cm^{-1} is not seen in the experiments. An asymmetric stretching of Zr−O in the [ZrO_6] cluster is observed at ~460 cm^{-1} (B_{1g}), which can be compared to the theoretical mode obtained at 522.21cm^{-1}. This mode has appeared at 515 cm^{-1} experimentally in previous works [76, 77]. Another asymmetric stretching of Zr-O in the [ZrO_6] cluster is observed at ~540 cm^{-1} (B_{2g}+ A_g), which is depicted in the lower part of **Fig. 7a** and can be compared to theoretical modes obtained at 537.44 and 544.99 cm^{-1}. Three theoretical stretching modes above 700 cm^{-1} are also obtained, which are not observed experimentally.

Fig. 7.

The higher stretching modes up to 480 cm^{-1} are depicted in **Fig. 7b** for the *t** state, while in **Table S1** (of Supporting Information), the corresponding values for the *s** state is also included for comparison purposes. In both cases, all the modes present A_g symmetry. An analysis of the results shows that the transformation from the fundamental *s* to *s** is produced by a slight distortion of the [ZrO_6] clusters. The orthorhombic form undergoes a displacive transition to a lower symmetry without bond breaking, which involves the structural order-disorder effect and can be associated to the Zr-O asymmetric stretching mode at 544.99 and 544.28 cm^{-1} for *s* and *s**, respectively. On the other hand, the transition from *s** to *t** excited electronic states can associated to vibrational movements along 544.28 cm^{-1} and 541,99 cm^{-1} for *s** and *t**, respectively. However, it is important to note that the pathways to reach both *s** and *t** electronic state imply a new spin rearrangement which supports a structural distortion resulting in new electronic configurations.

Optical properties such as PL are strongly dependent upon the structural and morphological features of the crystal system. Structural order–disorder associated effects are a crucial factor in determining the optical behavior of a material [78, 79]. During the PL process, a symmetry breaking occurs at short order involving two clusters, i.e., structural distortions associated with the imperfect coordination mainly related to the Zr sites. Then, the under-coordination associated with distorted [ZrO_6] and [CaO_{6+2}] clusters appear. The electron distribution is useful to predict the physical properties and it plays an important role in determining the lattice structure, the DOSs,

and the charge density. These structural and electronic changes can be related to the variation of polarization between distorted clusters that are capable of populating stable excited electronic states and hence result in active vibrational Raman modes. The triplet excited state has a higher energy than the excited singlet state; although the *s** state seems to be much more likely to occur, the two states would possibly be reached by irradiation during experimental measurements. Obviously, the decay process involves more than just two electrons, but in our model, two electrons per cell were used. In this study, we associate the experimental results related to characterization methods to theoretical results. On this basis, monitoring the energy and geometry of the singlet and triplet excited states will provide further insight into the PL mechanism. Furthermore, analyzing the relationship of these vibrations and geometries offers the opportunity to interpret the excited states in a new and possibly more intuitive way, linking electronic excitations with the concept of vibrational modes as being mainly responsible for PL behavior.

3.4.2 Band Structure and Density of States

The electron distribution plays an important role in determining the lattice structure, the DOS, and the charge density. The band structures plotted along the path Γ, Y, X, S, Z, T, U, R, and Γ for the *s, s**, and *t** electronic states, are depicted in **Figs. 8a-c**.

Fig. 8.

The band structure observed in **Fig. 8a-c** reveals a new configuration from spin alpha to spin beta, with a notable reduction of the energy gap value (from 6.23 eV in s and 6.14 eV in s* to 3.5 eV in t*). In order to understand the electronic structure of the CZO powders, the ground- and excited-density of states (DOS) are calculated. The total DOS and projection on atoms is shown in **Figs. 9a–c**, where the electronic contributions of the atoms in CZO can be noted in the *s, s**, and *t**states, respectively. In addition, the electronic contributions of the atomic orbitals are presented in **Figs. 10a–c** for the *s, s**, and *t** states, respectively.

Figs. 9.

Analysis of the electronic structure of the *s, s**, and *t** states (**Figs. 9** and **10**) demonstrated that the upper valence band is predominantly formed by the 2p (p_x, p_y, p_z)

states of all the O atoms in the cell and the bottom of the conduction band is mainly formed by the 4d (d_{xz}, d_{xy}, d_{yz}, d_{z2}, d_{x2-y2}) states of the Zr atom. (**Figs. 10a** and **b**) indicates that the *s* and *s** state presents an orthorhombic structure with the Zr atomic orbitals described as $4d_{z2}$, $4d_{yz}$, and $4d_{xy}$with a band gap value of 6.23 and 6.14 eV, respectively.

For the *t** state, the displacement of the Zr atom causes a slight distortion of the Zr4-O6, Zr4-O10, and Zr2-O10 bonds (as seen in **Table 1**), leading to the creation of localized states and a decrease in the gap energy. The calculated gap energy for this model alpha-beta is 3.5 eV.

Figs. 10.

The DOS in **Fig. 10b** reveals that these localized states are of 2p character, arising mainly from the 2p states of the oxygen O1 and O2, which are loosely connected to the Zr atom. This can be explained due to the asymmetry generated by the displacement of Zr along the z-axis.

The aforementioned experimental and theoretical results strongly indicate that PL is related to the structural short and long range order in the lattice. X-ray diffraction patterns showed a progressive structural disorganization of the powders milled for different times. The PL intensity increases when the powder is submitted at high temperature and its optical E_{gap} value decreases. This disorder caused in the system is a favorable condition to generate an intense and broad PL band. In this context, the results obtained for the triplet state indicate the existence of energy levels in the gap region, which decrease the value of the band gap and enable PL emissions.

3.5. Morphology Study

A study of the morphology of CZO in the *s* and *t** states is presented in **Figs. 11a** and **b**, respectively. The variation in the equilibrium shapes for these systems using the Wulff construction is a powerful tool to evaluate the morphology. When the relative stability of the facets changes (increases or decreases), more than one type of facet can appear in the resulting morphology, producing variations. Surface energy values for the studied surfaces of the CZO system in *s* and *t** are listed in **Table 3**. An analysis of the theoretical results indicates that the most stable surfaces in the singlet state are the (121), (100), (010), (101), (001), (111), and (011) facets, and the ideal morphology of

CZO is controlled by the (121), (100), (101), (001), and (010) facets (**Fig. 11a**). In the case of the triplet state, the thickness of the modeled surfaces have been reduced to the middle due to the computational cost, and the order of stability is (121), (101), (001), (100), (001), (111), and (011) facets, and the ideal morphology is controlled by the (121), (101), (100), and (001) facets (**Fig. 11b**).

Fig. 11.

Table 3.

We proposed the hypothesis that the decrease/increase of the surface energy in the triplet state with respect to the singlet state is due to the coordination of the O-Ca and O-Zr atoms, which are more exposed at the surfaces. **Fig. 12** shows a comparison of the triplet and singlet surfaces studied in this paper, showing the more exposed metallic clusters for both systems. In addition, the spin density localized in the triplet surfaces is included. All singlet and triplet surfaces are Ca-O terminated and [CaO_4] or [CaO_5] clusters are obtained for the two configurations. The main difference is the change from [CaO_5] to [CaO_4] in passing from *s* to *t** state for the (121) and (101) surfaces. In the case of Zr coordination, [ZrO_5] clusters are obtained in both the configurations, except for (121) in *t** in which Zr is four-coordinated.

Fig. 12.

A little modification in the order of stability between the singlet and triplet states occurs due to the contributions of different atoms in each surface of the material. In the triplet state the (121), (101), (100), and (001) surfaces have similar values of E_{surf}, which have strong influence on the triplet morphology. The (010) surface does not appear in the ideal triplet morphology since its E_{surf} value is less stable than in the singlet system. In addition, the E_{surf} values for the (101) and (121) planes are identical, showing a similar percentage of area in the triplet morphology, compared to the singlet.

It is worth noting that the (101) slab cut is produced along the shortest distance between the oxygen and zirconium (1.995 Å) and also along the greater distance of the O-Zr and O-Ca bond distances of 2.294 and 2.998 Å, respectively. The analysis of these results shows that the present equilibrium morphology is consistent with the atomic configurations and the local coordination of atoms for each surface.

The ground-state properties of solid materials are of obvious importance for establishing their structure, stability, and processing. However, the description of processes such as PL emissions requires a detailed characterization of the electronic

excited states properties. Elucidating their properties from first principles, on the basis of the constituent atoms and the laws of quantum mechanics, has long been a goal of theoretical and computational materials chemistry [80, 81]. A note of caution is mandatory here, on this methodological aspect. While the hybrid methods show good results for ground state properties, their performance for excited states is less satisfactory [82]. Electronic excited-state calculations for periodic systems are challenges in quantum chemistry because it is still very difficult to apply these methods to large/very large systems due to the steep scaling in the number of electrons. In the present work, the excited states have been localized and characterized at the DFT calculation level. This is a strong constraint and from the computational point of view, and represents a technical problem, since to obtain more accurate geometries and electronic properties of the excited states, it is necessary to use more sophisticated and demanding quantum calculations, such as multiconfiguration-based methods or by using the many-body perturbation theory. In this contribution, we do not aim at providing an exact application of DFT calculation, but rather to give a flavor of today possibilities. Methodological developments are mandatory in this context, along with new approaches, to calculate accurately values of band gaps and charge transfer excitations.

4. Conclusions

Modern physics relies heavily on the concepts of classical solid state physics with its emphasis on ideal infinite crystals and perfect symmetries. Real materials are not perfect crystals; they contain a number of defects and lattice imperfections, which are responsible for the properties of the materials. Therefore, in some cases, the reliability of a physical model rather than the precision of mathematical equations should be emphasized if one needs to investigate real materials. In this context, theoretical characterization of the geometrical and electronic structures of ground and excited electronic states can complement experiments inherently limited by equipment accuracy. A theoretical framework to interpret PL emissions, based on the localization and characterization of the nature for the ground, *s*, and excited (singlet, *s**, and triplet, *t**) electronic states, using ideal and distorted periodic supercell models of CZO, has been developed. Their corresponding geometries, electronic structures, and vibrational frequencies were obtained.

In this work, $CaZrO_3$ powders were prepared by the polymeric precursor method. Their structural and electronic properties have been studied previously [58], while the PL properties of crystalline CZO were investigated herein. The techniques of X-ray diffraction (XRD), Raman spectra, and PL spectroscopy at room temperature were used for characterization. XRD patterns indicated a pure orthorhombic perovskite phase of $CaZrO_3$ at synthesis temperatures of 400, 600, 800, and 1000 °C. Raman spectra and XRD patterns reported long- and short-range order at 1000 °C.

First principle calculations reveal that the intensity of PL emissions is attributed to structural order-disorder effects related to the polyhedral distortion, i.e. the modification of geometric and electronic structure of both $[ZrO_6]$ and $[CaO_8]$ clusters in the electronically excited states, generating electronic levels located between the valence and conduction bands, which are basically composed of O 2p orbitals (valence band) and Zr 4d orbitals (conduction band). The band structures and the density of states revealed energy gap values of 6.23, 6.14, and 3.50 eV for the *s*, *s** and *t** electronic states, with the process of breaking of symmetry being a necessary condition for the existence of energy levels in the forbidden region of the band gap. The structural order-disorder effect on the coordination of $[ZrO_6]$ and $[CaO_8]$ clusters is demonstrated by theoretical calculations, as well as the shallow defect states found in the morphologies, where the local coordination of exposed atoms for each surface can be related to the order of surface energy stability. A little modification in the order of stability of surfaces occurs between the singlet and triplet states, generating differences in their corresponding morphologies.

To conclude, in this study, we present a general description of excited electronic states of CZO, thereby shedding light on the complex interplay between structural order-disorder effects and PL emissions, which is a challenging field of study both experimentally and intellectually. This technique can be used to extract chemical shifts for the structural characterization of excited states and to elucidate complex excited states. Finally, we need to recognize that present DFT calculations show limitations inherent in current exchange-correlation functional.

ACKNOWLEDGEMENTS

The authors acknowledge the financial support of the agencies: Generalitat Valenciana for PrometeoII/2014/022 and ACOMP/2014/270, ACOMP/2015/1202, Ministerio de Economia y Competitividad, project CTQ2015-65207-P, and Programa de Cooperación Científica con Iberoamerica (Brasil) of Ministerio de Educación (PHBP14-00020). J.A. acknowledges the Ministerio de Economia y Competitividad, "Salvador Madariaga" program, PRX15/00261. M.C.O acknowledges Generalitat Valencia for the Santiago Grisolia program 2015/033.

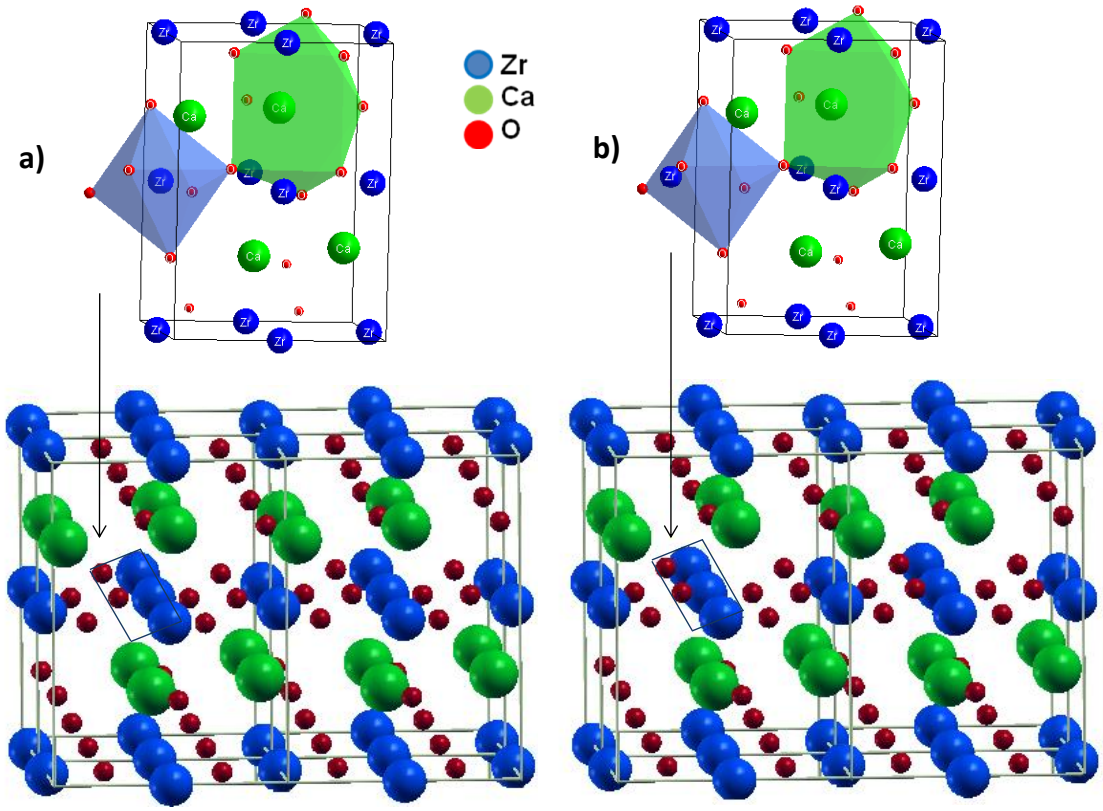

Figure 1. Cell 1x1x1 for modelling the electronic states of CZO and the corresponding expansion by periodicity: a) singlet electronic state, s, and b) excited singlet, s*, and triplet, t*, electronic states.

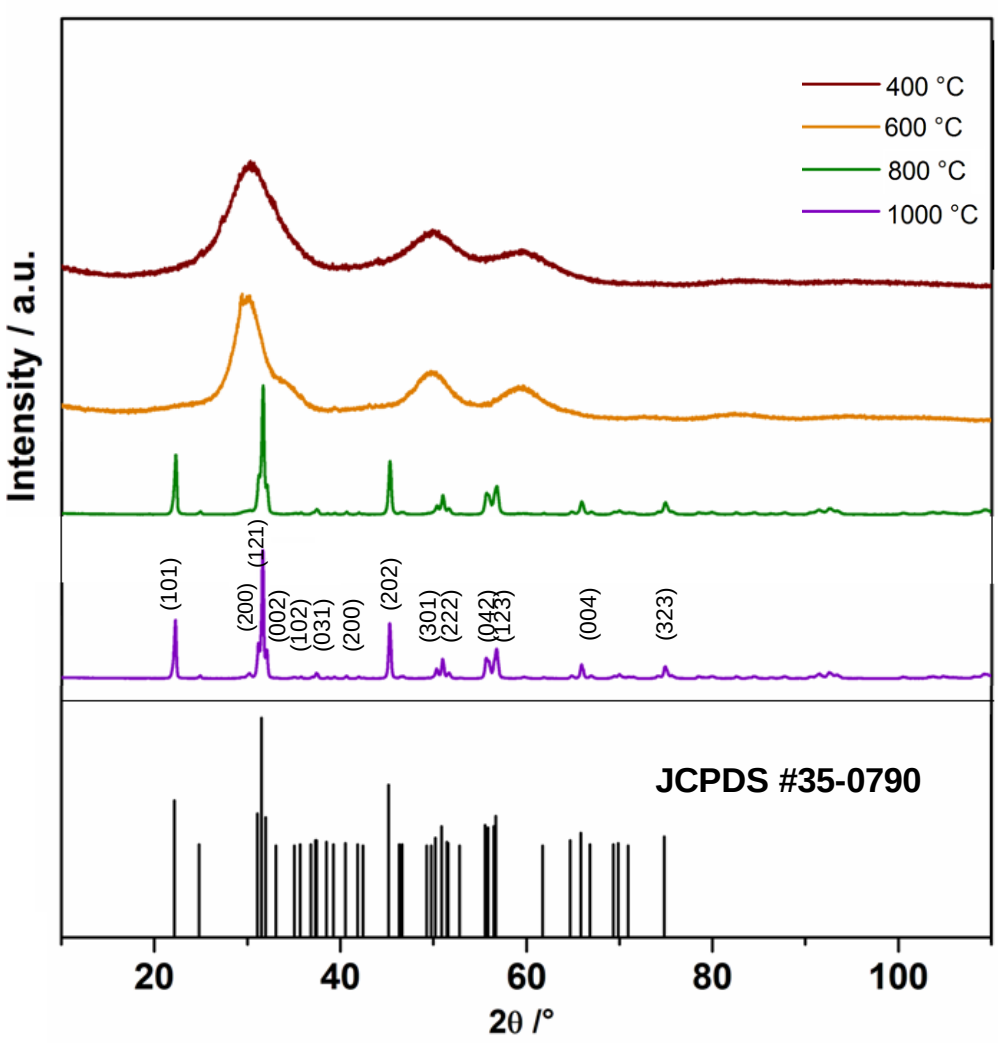

Figure 2. XRD patterns (room temperature) of the CZO powders synthesized at different temperatures for 2h.

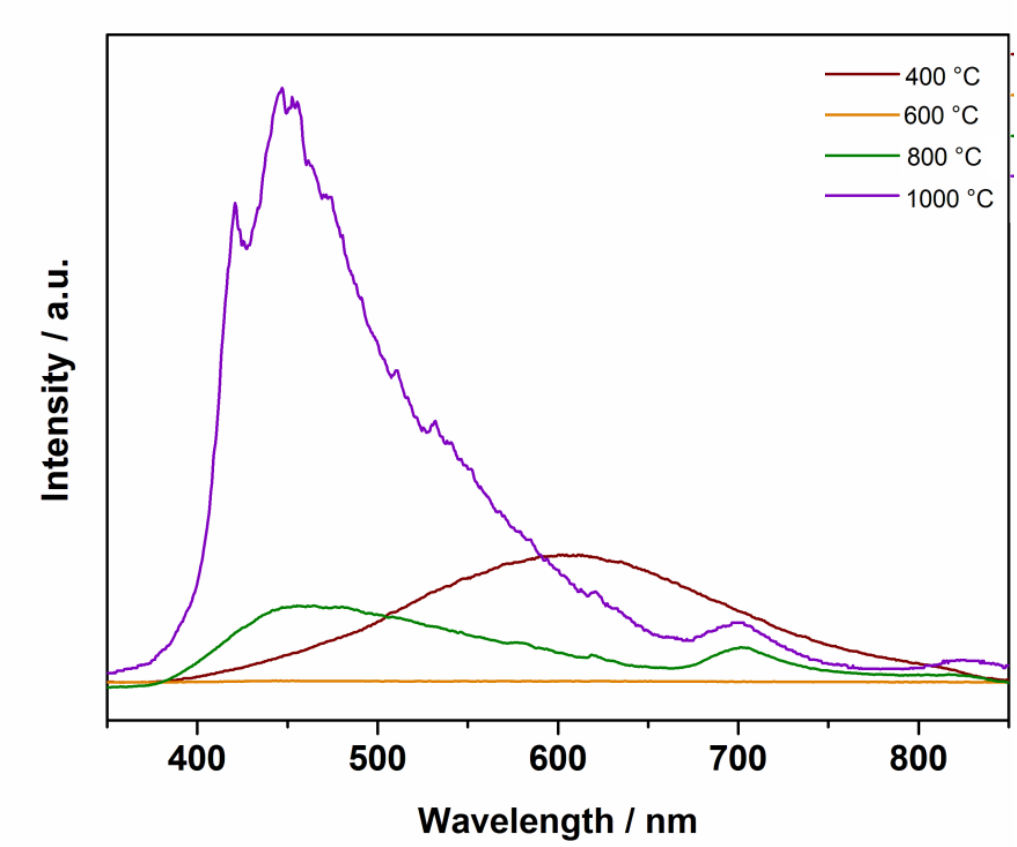

Figure 3. Photoluminescence spectra (room temperature) of the CZO powder synthesized at different temperatures.

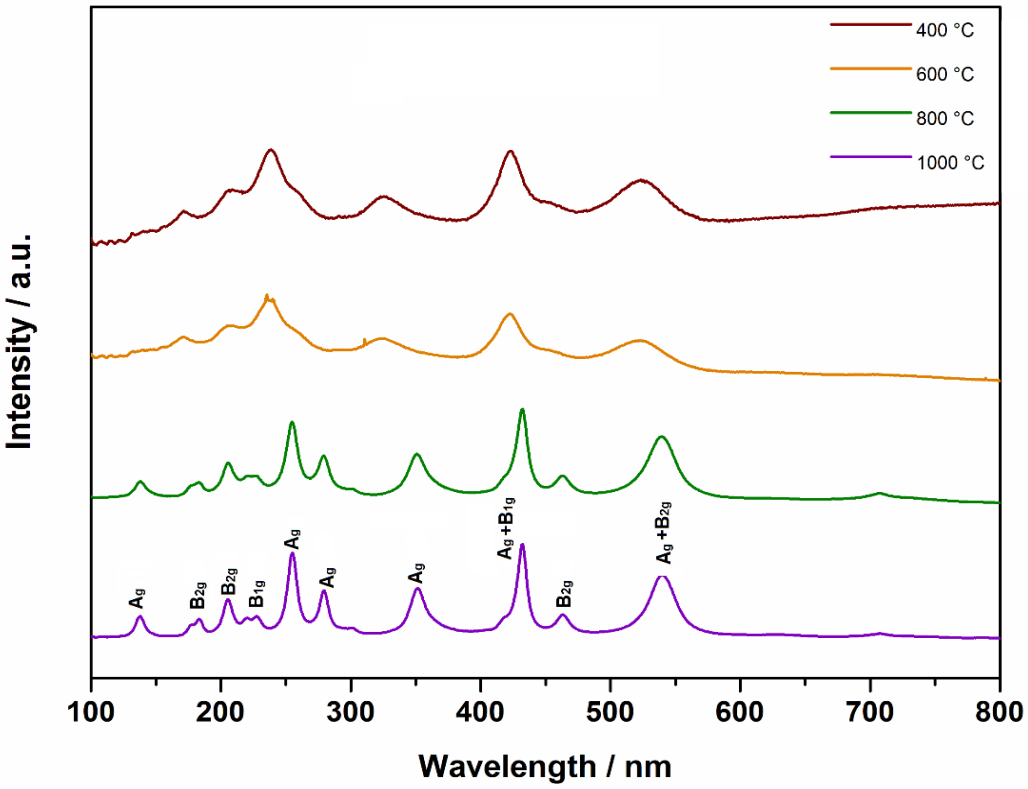

Figure 4. Raman spectra (room temperature) of CZO powder synthesized at different temperatures. The positions of the active modes are indicated.

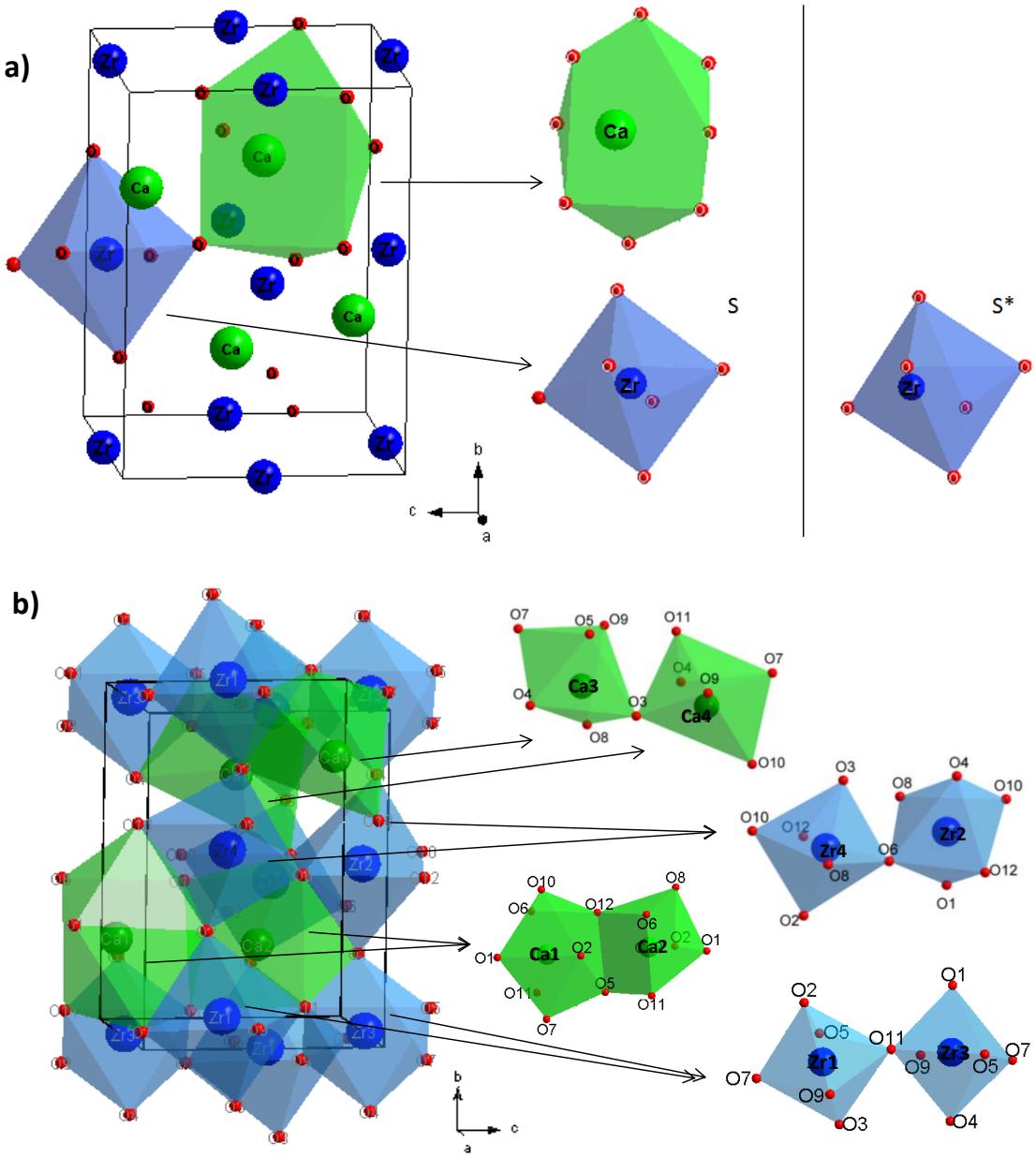

Figure 5. Electronic states of CZO in terms of cluster constituents: a) singlet and excited singlet electronic states, s and s*, respectively and b) excited triplet electronic state, t*.

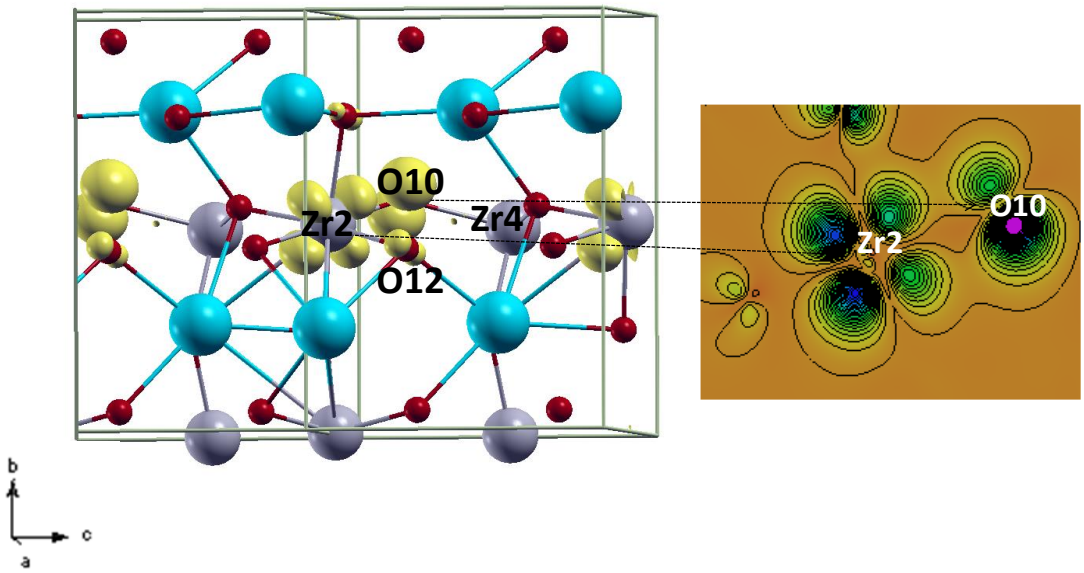

Figure 6. Spin density localization for the t* state of CZO: a) 3D representation where the spin density is localized (yellow color) in $4d_{z^2}$, $4d_{yz}$ and $4d_{xy}$ of Zr2 atom and $2p_z$ of O10 atom. b) Projection on a plane (passing through Zr2-O10-O12 atoms) in which atoms with highest spin density are included.

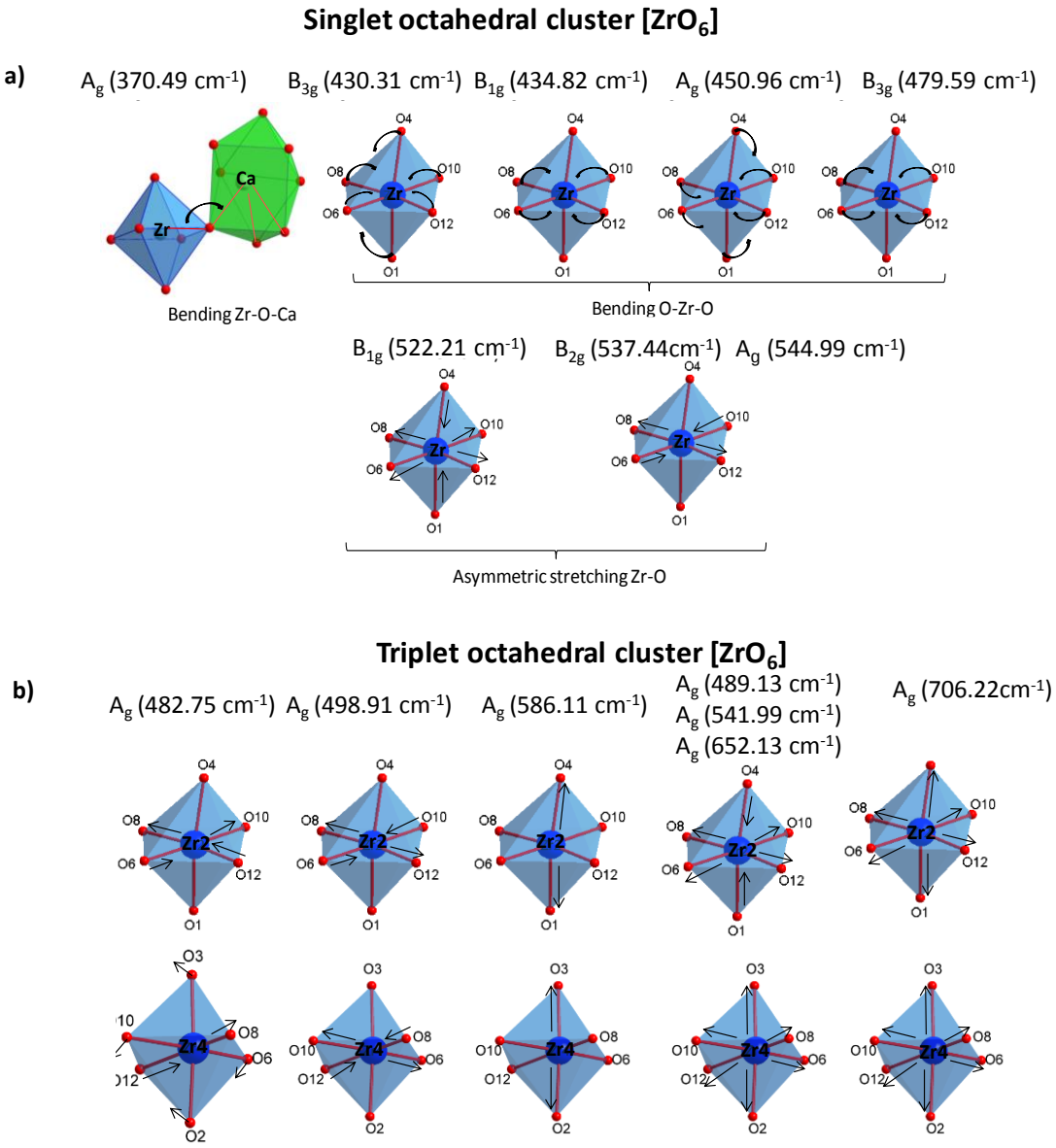

Figure 7. Theoretical Raman active modes of CZO crystal involving octahderal [ZrO_6] cluster : a) singlet fundamental state, s, and b) triplet excited state, t*.

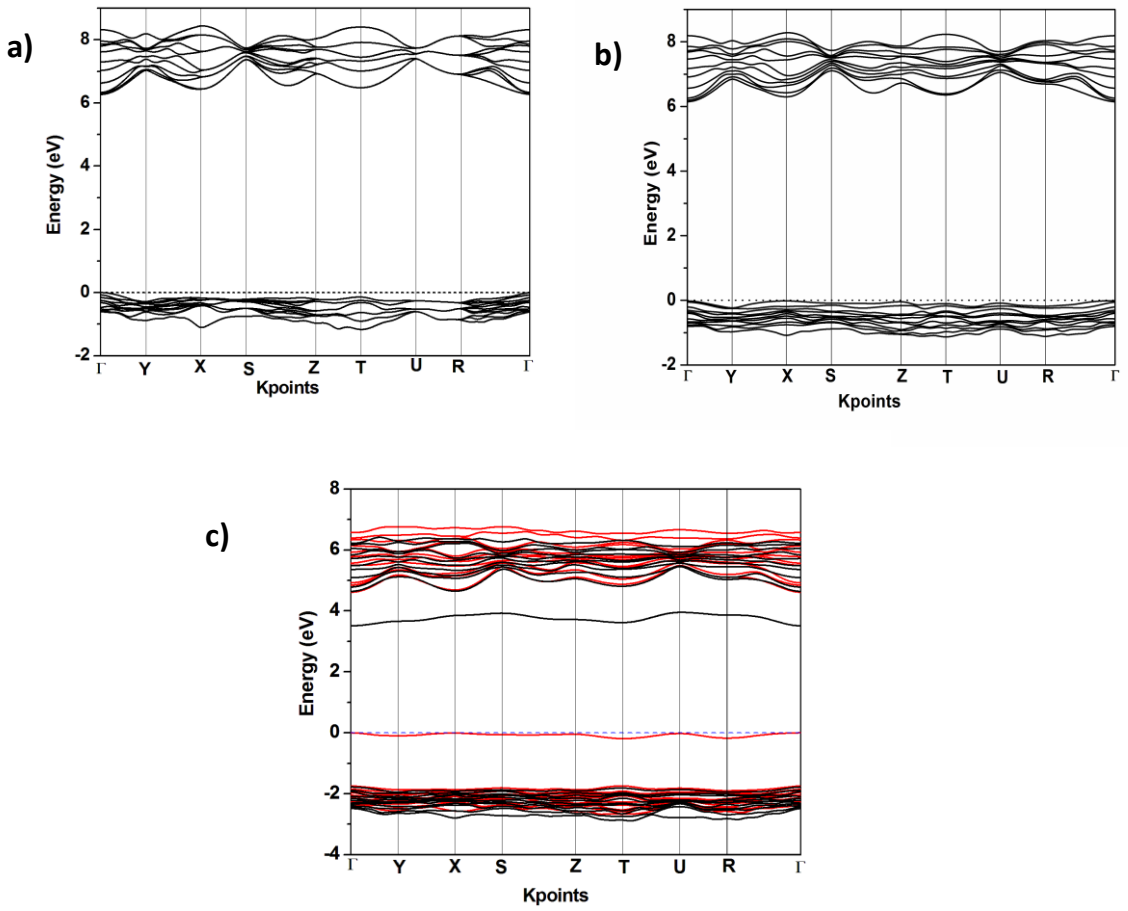

Figure 8. Band structure of CZO: a) s, b) s* and c) t* electronic states.

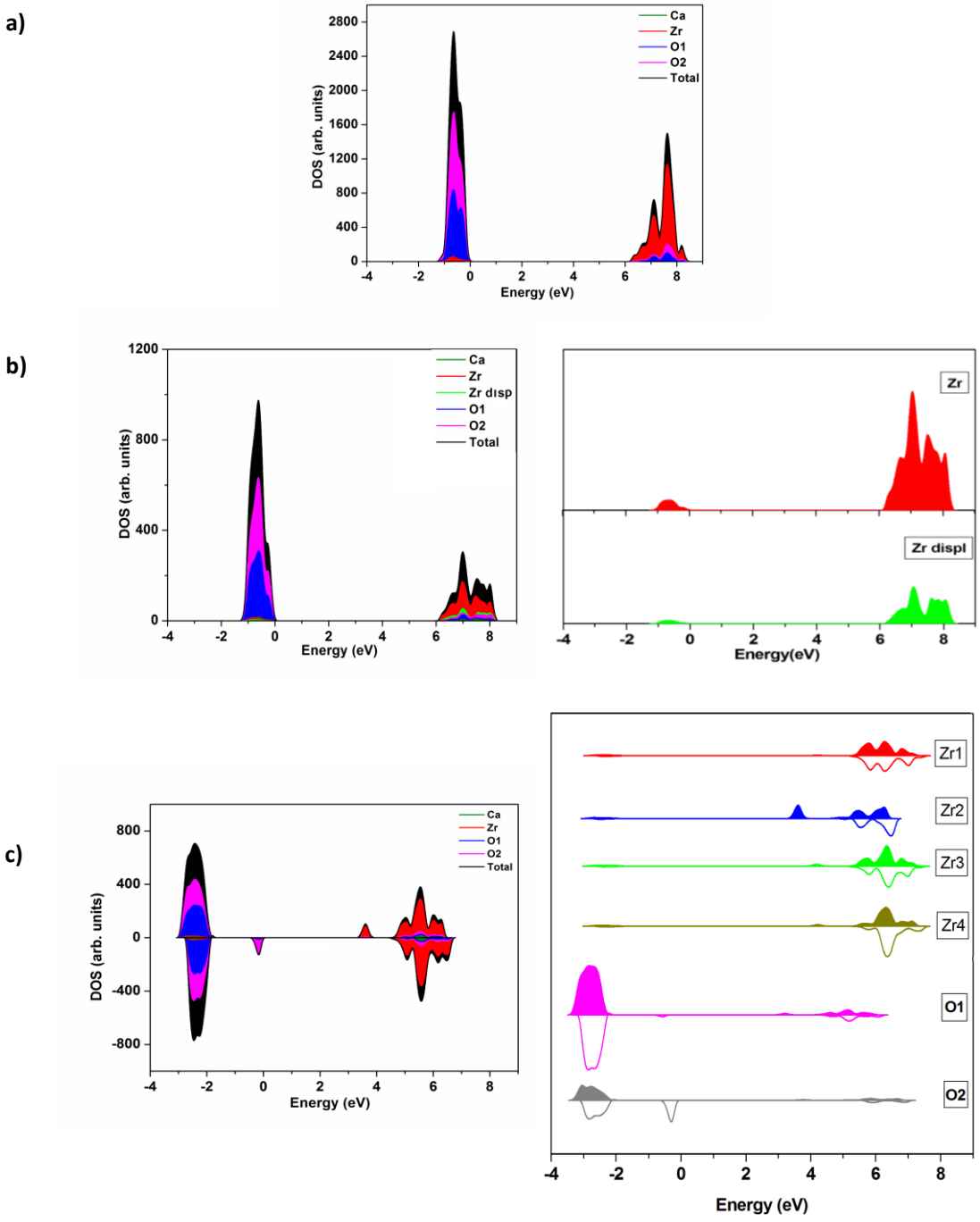

Figure 9. Total and projected DOS on atoms for CZO: a) s, b) s* and c) t* electronic states.

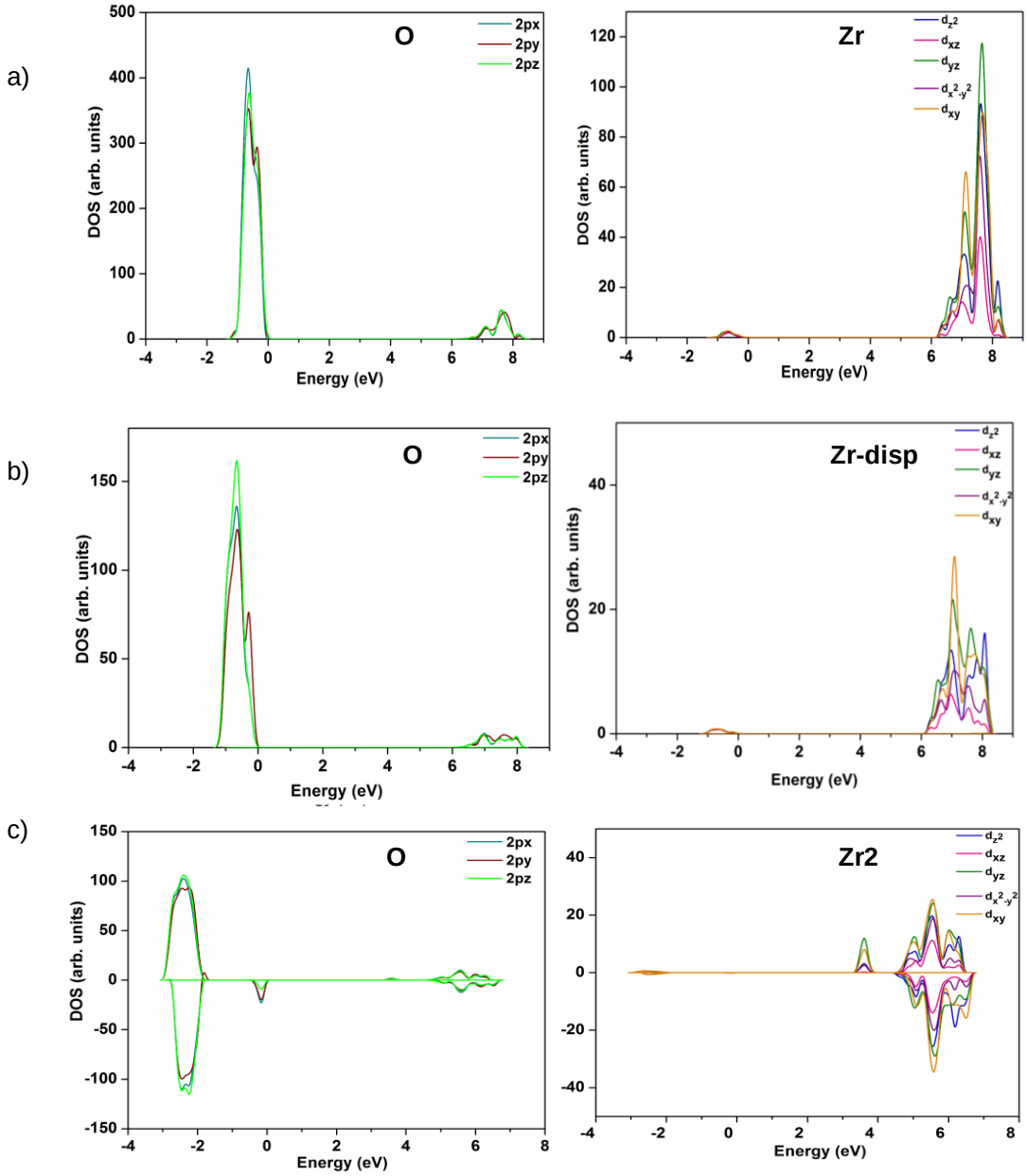

Figure 10. DOS projected on orbitals CZO: a) *s* b) *s**and c) *t** electronic states.

a)

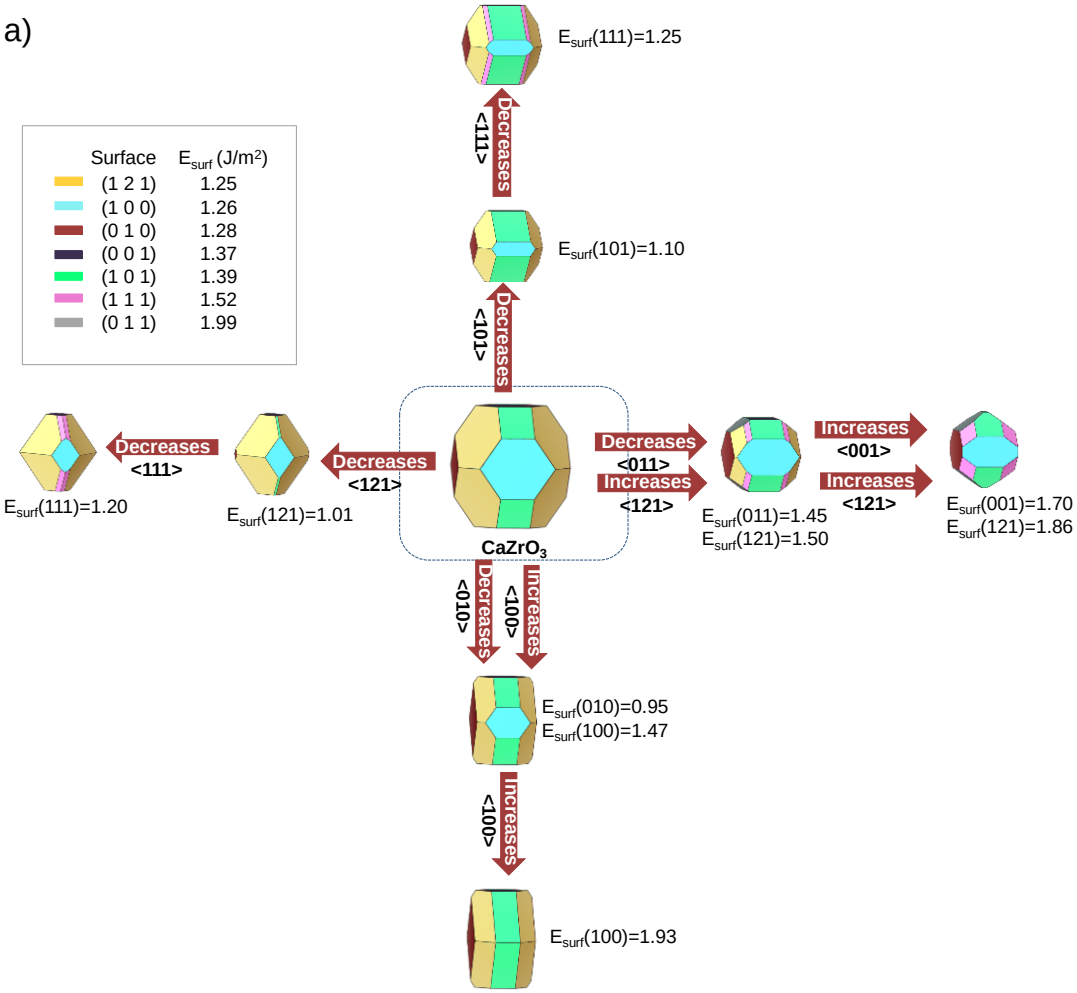
Surface
E_{surf} (J/m²)
(1 2 1) 1.25
(1 0 0) 1.26
(0 1 0) 1.28
(0 0 1) 1.37
(1 0 1) 1.39
(1 1 1) 1.52
(0 1 1) 1.99
E_{surf}(111)=1.25
Decreases <111>
E_{surf}(101)=1.10
Decreases <101>
Decreases <111>
E_{surf}(111)=1.20
Decreases <121>
E_{surf}(121)=1.01
CaZrO3
Decreases <011>
Increases <121>
E_{surf}(011)=1.45
E_{surf}(121)=1.50
Increases <001>
Increases <121>
E_{surf}(001)=1.70
E_{surf}(121)=1.86
Decreases <010>
Increases <100>
E_{surf}(010)=0.95
E_{surf}(100)=1.47
Increases <100>
E_{surf}(100)=1.93

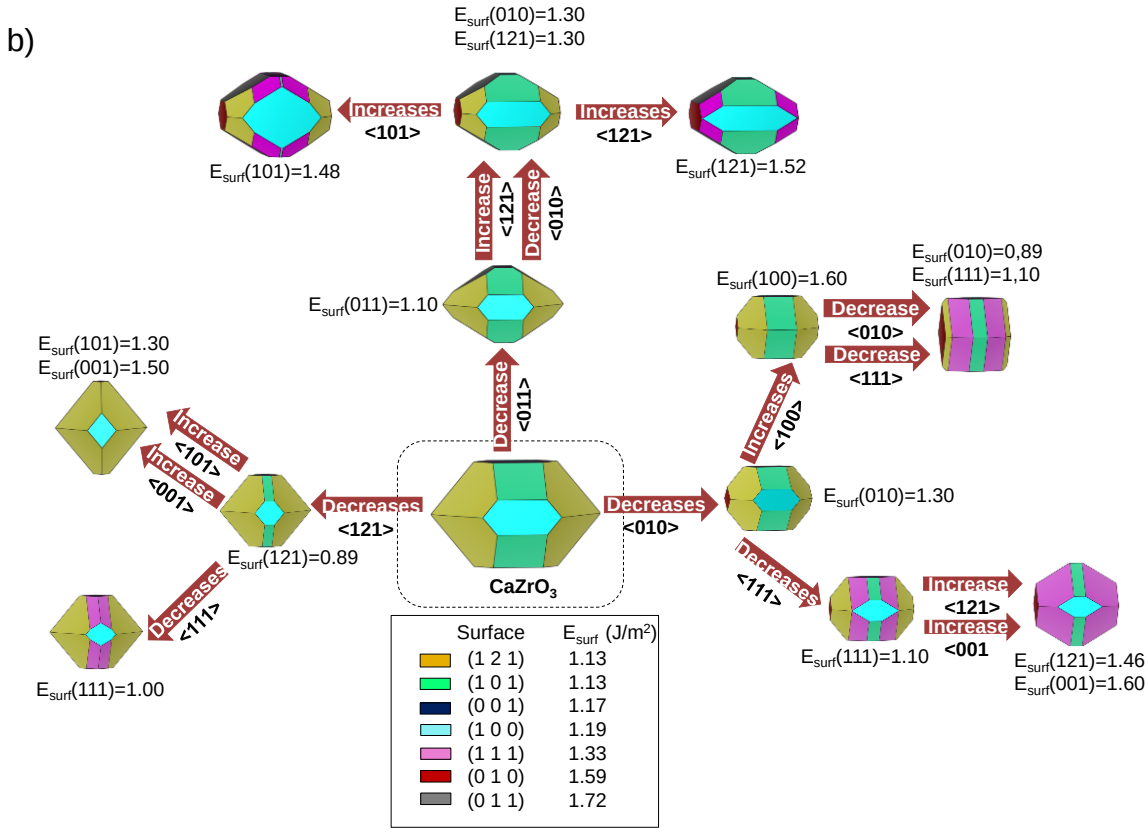

Figure 11. Morphologies of CZO: a) s and b) t*electronic states.

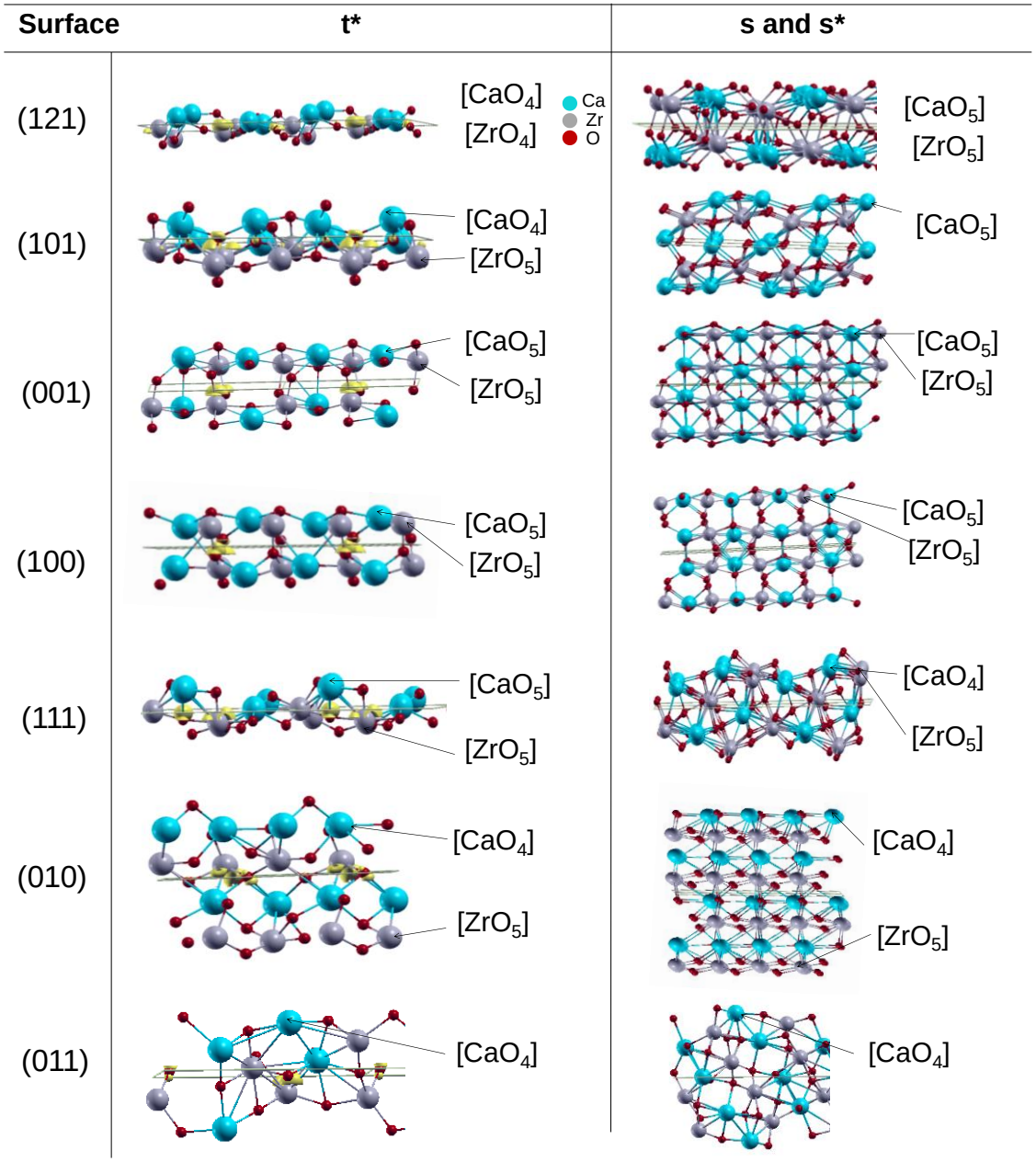

Figure 12. A schematic representation for the surfaces of t* state of CZO where the spin density (in yellow) is depicted. The most external clusters for t* and s and s* states are indicated.

Table 1. Bond distances for the fundamental singlet electronic state (s) and excited (s*) and triplet (t*) electronic states 1x and 2x refers to the multiplicity of the bond.

s				t*					
Bond			**(Å)**	**Bond**			**(Å)**	**Bond**	**(Å)**
Ca	O1	1x	2.341	**Ca1**	O1		2.352	**Ca2**O2	2.348
	O2	2x	2.362		O11		2.368	O12	2.433
	O1	1x	2.461		O6		2.371	O1	2.447
	O2	2x	2.679		O2		2.425	O5	2.449
	O2	2x	2.844		O12		2.571	O8	2.583
					O5		2.749	O6	2.669
					O7		2.823	O9	3.050
					O10		2.906	O11	2.814
				Ca3	O3		2.320	**Ca4**O4	2.301
					O9		2.364	O7	2.346
					O8		2.369	O10	2.381
					O4		2.413	O3	2.408
					O5		2.667	O11	2.573
					O7		2.669	O9	2.656
					O10		2.998	O6	3.027
					O12		3.173	O8	3.272
Zr	O2	2x	2.100	**Zr1**	O9		2.102	**Zr2** O12	2.160
	O2	2x	2.091		O2		2.105	O6	2.171
	O1	2x	2.097		O7		2.105	O4	2.179
					O5		2.115	O8	2.190
s*					O11		2.159	O1	2.194
Bond			**(Å)**		O3		2.186	O10	2.292
Zr	O2	1x	1.657	**Zr3**	O1		2.074	**Zr4**O6	1.995
displ.	O2	1x	2.596		O9		2.111	O8	2.096
	O2	1x	1.839		O4		2.128	O3	2.128
	O2	1x	2.455		O7		2.147	O12	2.131
	O1	1x	2.232		O11		2.149	O2	2.174
	O1	1x	2.116		O5		2.157	O10	2.294

a=5.594 Å, b=8.021 Å and c=5.761 Å for s and s* states.
a=5.673 Å , b=8.155 Å and c=5.844 Å for t* state.

Table 2. Raman active modes for s electronic state, compared to experimental data at different temperatures of synthesis.

Theoretical			**Experimental**		
			Temperature (°C)		
Mode		Corrected*	400/600	800	1000
		υ (cm^{-1})			
A_g	127.82	120.15		137.90	137.90
B_{1g}	164.69	154.81			
B_{2g}	169.64	159.46	171.44	182.97	183.1
A_g	194.41	182.75			
B_{2g}	203.30	191.10	203.51	205.69	205.69
B_{2g}	225.97	212.41			
B_{2g}	227.59	213.93			
B_{1g}	246.54	231.75		225.91	227.56
A_g	280.77	263.92	238.50	255.26	255.26
A_g	296.77	278.96		279.32	279.32
B_{3g}	317.44	298.39			
B_{2g}	372.05	349.73			
B_{3g}	387.97	364.69			
A_g	394.14	370.49	324.91	351.49	351.49
B_{3g}	457.78	430.31			
B_{1g}	462.57	434.82	422.29	432.40	432.40
A_g	479.75	450.97			
B_{3g}	510.21	479.60			
B_{1g}	555.54	522.21			
B_{2g}	571.74	537.44		463.02	463.02
A_g	579.78	544.99	522.79	540.29	540.29
B_{2g}	737.33	693.09			
B_{3g}	797.02	749.20			
B_{1g}	808.01	759.53			

*0.94 = scaling factor

Table 3. Surface energy and band gap values for the (121), (100), (010), (101), (001), (111) and (011) surfaces of CZO crystals.

	s			t*		
Surface	**E_{suf} (J/m^2)**	**Area (Å)**	**E_{gap} (eV)**	**E_{suf} (J/m^2)**	**Area (Å)**	**E_{gap} (eV)**
(121)	1.25	91.13	6.61	1.13	93.28	4.21
(100)	1.26	44.21	6.41	1.19	47.66	4.53
(010)	1.28	32.23	5.62	1.59	33.15	4.66
(101)	1.39	64.41	6.39	1.13	66.00	4.95
(001)	1.37	44.87	6.28	1.17	46.27	4.61
(111)	1.52	72.03	5.64	1.33	73.68	4.75
(011)	1.99	55.25	5.69	1.72	56.73	4.07

References

[1] L. Pauling, J. Am. Chem. Soc., 51 (1929) 1010–1026.
[2] M.E. Lines, A.M. Glass, Principles and Applications of Ferroelectrics and Related Materials, Oxford Classic Texts in the Physical Sciences, 1977.
[3] A.E. Souza, G.S. Sasaki, S.A. Camacho, S.R. Teixeira, M.S. Li, E. Longo, J. Lumi., 179 (2016) 132-138.
[4] G. Blasse, Optical electron transfer between metal ions and its consequences, in: Complex Chemistry, Springer Berlin Heidelberg, Berlin, Heidelberg, 1991, pp. 153-187.
[5] E.S. Junior, F.A.L. Porta, M.S. Liu, J. Andrés, J.A. Varela, E. Longo, Dalton Trans., 44 (2015) 3159-3175
[6] F.A.L. Porta, J. Andres, M.V.G. Vismara, C.F.O. Graeff, J.R. Sambrano, M.S. Li, J.A. Varela, E. Longo, J. Mater. Chem. C, 2 (2014) 10164.
[7] F.A.L. Porta, J. Andrés, M.S. Li, J.R. Sambrano, J.A. Varela, E. Longo, Phys. Chem. Chem. Phys., 16 (2014) 20127-20137
[8] P.G. Mendes, M.L. Moreira, S.M. Tebcherani, M.O. Orlandi, J. Andrés, M.S. Li, N. Diaz-Mora, J.A. Varela, E. Longo, J. Nanopart ReS., 14 (2012) 750.
[9] M.R.D. Bomio, L.S. Cavalcante, M.A.P. Almeida, R.L. Tranquilin, N.C. Batista, P.S. Pizani, M.S. Li, J. Andres, E. Longo, Polyhedron, 50 (2013) 532-545.
[10] L.S. Cavalcante, E. Moraes, M.A.P. Almeida, C.J. Dalmaschio, N.C. Batista, J.A. Varela, E. Longo, M.S. Li, J. Andrés, A. Beltrán, Polyhedron, 54 (2013) 13-25.
[11] V.D. Araújo, R.L. Tranquilin, F.V. Motta, C.A. Paskocimas, M.I.B. Bernardi, L.S. Cavalcante, J. Andres, E. Longo, M.R.D. Bomio, Mater. Sci. Semicond. Process., 26 (2014) 425-430.
[12] F.M.C. Batista, F.A.L. Porta, L. Gracia, E. Cerdeiras, L. Mestres, M.S. Li, N.C. Batista, J. Andrés, E. Longo, L.S. Cavalcante, J. Mol. Struct., 1081 (2015) 381-388.
[13] Y.V.B.D. Santana, J.E.C. Gomes, L. Matos, G.H. Cruvinel, A. Perrin, C. Perrin, J. Andrès, J.A. Varela, E. Longo, Nanomater. Nanotechno., 4 (2014) 22.
[14] L.G. Tejuca, J.L. G.Fierro, J.M. D.Tascon, Structure and Reactivity of Perovskite-Type Oxides. In Advances in Catalysis, in: A. Press (Ed.), New York, 1989.
[15] R. Pazik, R. Tekoriute, S.H. kansson, R. Wiglusz, W. Strek, G.A. Seisenbaeva, Y.K. Gun'ko, V.G. Kessler, Chem. Eur. J., 15 (2009) 6820 – 6826.
[16] J.A. Enterkin, W. Setthapun, J.W. Elam, S.T. Christensen, F.A. Rabuffetti, L.D. Marks, P.C. Stair, K.R. Poeppelmeier, C.L. Marshall, ACS Catal., 1 (2011) 629–635.
[17] J. Andres, V.M. Longo, L.S. Cavalcante, M.L. Moreira, J.A. Varela, E. Longo, A Fresh Look at the Structural, Ferroelectric and Photoluminescent Properties in Perovskites, 1 ed., Photoluminescence: Applications, Types and Efficacy, New York - United States, 2012.
[18] M. Misono, Stud. Surf. Sci. Catal., 176 (2013) 67-95.
[19] L. Bia, E. Traversa, J. Mater. Res., 29 (2014) 1-15.
[20] W. Wang, M. O.Tadé, Z. Shao, Chem. Soc. Rev., 44 (2015) 5371-5408.
[21] E. Grabowska, Appl. Catal. B, 186 (2016) 97–126.
[22] J.F. Nye, Physical Properties of Crystals: Their Representation by Tensors and Matrices, Oxford: Clarendon Press, New York, 1985.
[23] A.M. Glazer, Acta Crystallogr. Sect. A: Cryst. Phys. Diffr. Theor. Gen. Crystallogr., 31 (1975) 756-762.
[24] A.M. Glazer, Acta Cryst., B28 (1972) 3384-3392.
[25] U. Lüdersa, Q.-R. Lia, R. Feyerhermb, E. Dudzikb, J. Phys. Chem. Solids, 75 (2014) 1354–1360.
[26] I. Qasim, P.E.R. Blanchard, S. Liu, C. Tang, B.J. Kennedy, M. Avdeev, J.A. Kimpton, J. Solid State Chem., 206 (2013) 242-250.

[27] V.M. Longo, L.S. Cavalcante, M.G.S. Costa, M.L. Moreira, A.T. de Figueiredo, J. Andrés, J.A. Varela, E. Longo, Theoretical Chemistry Accounts, 124 (2009) 385.
[28] S.d. Lazaro, J. Milanez, A.T.d. Figueiredo, V.M. Longo, V.R. Mastelaro, F.S.D. Vicente, A.C. Hernandes, J.A. Varela, E. Longo, Appl. Phys. Lett, 90 (2007) 111904.
[29] M. Anicete-Santos, M.S. Silva, E. Orhan, M.S. Góes, M.A. Zaghete, C.O. Paiva-Santos, P.S. Pizani, M. Cilense, J.A. Varela, E. Longo, J. Lumin., 127 (2007) 689-695.
[30] M. Anicete-Santos, R.C. Lima, E. Orhan, M.A.M.A. Maurera, L.G.P. Simões, G. Souza, P.S. PIZANI, E.R. Leite, J.A. Varela, E. Longo, J. Computer-Aided Mater. Des., 12 (2005) 111–119.
[31] L. Gracia, J. Andrés, V.M. Longo, J.A. Varela, E. Longo, Chem. Phys. Lett., 493 (2010) 141-146.
[32] L.F. da Silva, J.-C. M'Peko, J. Andrés, A. Beltrán, L. Gracia, M.I.B. Bernardi, A. Mesquita, E. Antonelli, M.L. Moreira, V.R. Mastelaro, The Journal of Physical Chemistry C, 118 (2014) 4930-4940.
[33] V.M. Longo, M.d.G.S. Costa, A.Z. Simões, I.L.V. Rosa, C.O.P. Santos, J. Andrés, E. Longo, J.A. Varela, Phys. Chem. Chem. Phys, 12 (2010) 7566-7579
[34] L. Gracia, V. M. Longo, L. S. Cavalcante, A. Beltrán, W. Avansi, M. S. Li, V. R. Mastelaro, J. A. Varela, E. Longo, J. Andrés, J. Appl. Phys., 110 (2011) 043501.
[35] M.L. Moreira, P.G.C. Buzolin, V.M. Longo, N.H. Nicoleti, J.R. Sambrano, M.S. Li, J.A. Varela, E. Longo, J. Phys. Chem. A, 115 (2011) 4482–4490
[36] M.L. Moreira, J. Andrés, L. Gracia, A. Beltrán, L.A. Montoro, J.A. Varela, E. Longo, J. Appl. Phys., 114 (2013) 043714
[37] R. Uarth Fassbender, T. Strelow Lilge, S. Cava, J. Andres, L. Fernando da Silva, V. Roberto Mastelaro, E. Longo, M. Lucio Moreira, Physical Chemistry Chemical Physics, 17 (2015) 11341-11349.
[38] R.S. André, S.M. Zanetti, J.A. Varela, E. Longo, Ceram. Int., 40 (2014) 16627-16634.
[39] X. Liu, J. Zhang, X. Ma, H. Sheng, P. Feng, L. Shi, R. Hu, Y. Wang, J. Alloy. Compd., 550 (2013) 451-458.
[40] Y. Shimizu, S. Sakagami, K. Goto, Y. Nakachi, K. Ueda, Mat. Sci. Eng. B, 1611 (2009) 100-103.
[41] H.W. Zhang, X.Y. Fu, S.Y. Niu, Q. Xin, J. Lumi., 128 (2008) 1348-1352.
[42] H. Zhang, X. Fu, S. Niu, Q. Xin, J. Alloy. Compd., 459 (2008) 103-106.
[43] H. Wang, M. Wang, W. Zhang, N. Zhao, W. Wei, Y. Sun, Catal. Today, 115 (2006) 107-110.
[44] M. Pollet, S. Marinel, J. Mater. Sci., 39 (2004) 1943-1958.
[45] G. Róg, M. Dudek, A. Kozłowska-Róg, M. Bućko, Electrochim. Acta, 47 (2002) 4523-4529.
[46] M.S. Islam, R.A. Davies, J.D. Gale, Chem. Mater., 13 (2001) 2049-2055.
[47] K. Kobayashi, S. Yamaguchi, Y. Iguchi, Solid State Ionics, 108 (1998) 355-362.
[48] H. Iwahara, T. Yajima, T. Hibino, K. Ozaki, H. Suzuki, Solid State Ionics, 61 (1993) 65-69.
[49] S. Sakaida, Y. Shimokawa, T. Asaka, S. Honda, Y. Iwamoto, Mater. Res. Bull., 67 (2015) 146-151.
[50] H. J. A. Koopmans, G. M. H. V. Velde, P. J. Gellings, Acta Cryst., C39 (1983) 1323-1325.
[51] M. Dudek, E. Drożdż-Cieśla, J. Alloy. Compd., 475 (2009) 846-854.
[52] P. Stoch, J. Szczerba, J. Lis, D. Madej, Z. Pędzich, J. Eur. Ceram. Soc., 32 (2012) 665-670.
[53] M.G. Brik, C.-G. Ma, V. Krasnenko, Surf. Sci., 608 (2013) 146-153.
[54] A.L. Ibiapino, L.P. Figueiredo, G.E. Lascalea, R.J. Prado, Quím. Nova 36 (2013) 762-767.
[55] Z. F. Hou, Physica B-Condensed. Matter., 403 (2013) 2624-2628.
[56] S.K. Gupta, P.S. Ghosh, N. Pathak, R. Tewari, RSC Advances, 5 (2015) 56526-56533.
[57] R.A. Gouvêa, E.M. Flores, S.d.S. Cava, M.L. Moreira, Journal of Luminescence, 180 (2016) 73-80.
[58] I.L.V. Rosa, M.C.Oliveira, M.Assis, M.Ferrer, R.S.André, E.Longo, M.F.C.Gurgel, Ceram. Int., 41 (2015) 3069–3074.
[59] A.C.V.D. LARSON, R. B., General Structure Analysis System (GSAS) program, in, Los Alamos, NM, Rep. N°. LAUR 86–748, Los Alamos National Laboratory, University of California., 2004.

[60] W. Finger, D.E. Cox, A.P. Jephcoat, J. Appl. Cryst., 27 (1994) 892-900.
[61] I.L.V. Rosa, M.C.Oliveira, M.Assis, M.Ferrer, R.S.André, E.Longo, M.F.C.Gurgel, Ceramics International, 41 (2015) 3069–3074.
[62] V.R.S. R. Dovesi, C. Roetti, R. Orlando, C. M. Zicovich-Wilson, F. Pascale, B. Civalleri, K. Doll, N.M. Harrison, I.J. Bush, Ph. D'Arco, M. Llunel, M. Caus`a, Y. No¨e, CRYSTAL14, in: U.O. Torino (Ed.), Torino- Italy, 2014.
[63] C.T. Lee, W.T. Yang, R.G. Parr, Phys. Rev. B: Condens. Matter, 37 (1988) 785.
[64] A.D. Becke, J. Chem. Phys, 98 (1993) 5648.
[65] E. Longo, E. Orhan, F.M. Pontes, C.D. Pinheiro, E.R. Leite, J.A. Varela, P.S. Pizani, T.M. Boschi, J. F. Lanciotti, A. Beltrán, J. Andrés, Phys. Rev. B 69 (2004) 125115.
[66] L. Valenzano, F.J. Torres, K. Doll, F. Pascale, C.M. Zicovich-Wilson, R. Dovesi, Z. Phys. Chem., 220 (2006) 893-912.
[67] L. Valenzano, B. Civalleri, S. Chavan, S. Bordiga, M. Nilsen, S. Jakobsen, K.P. Lillerud, C. Lamberti, Chem. Mater. , 23 (2011) 1700-1718.
[68] F. Cora, Mol. Phys. , 103 (2005) 2483-2496
[69] H.J. Monkhorst, J.D. Pack, Physical review B, 13 (1976) 5188.
[70] K.P. Balashev, Koord. Khim, 15 (1989) 116-121.
[71] J.B. Foresman, E. Frisch, Exploring Chemistry with Electronic Structure Methods, in: Frequency Calculations. Gaussian, Inc., Pittsburgh. P.A, 1996, pp. 61-90.
[72] M.F.C. Gurgel, M.L. Moreira, E.C. Paris, J.W.M. Espinosa, P.S. Pizani, J.A. Varela, E. Longo, International Journal of Quantum Chemistry, 111 (2011) 694-701.
[73] V.M. Orera, C. Pecharroman, J.I. Pena, R.I. Merino, C.J. Serna, J. Phys. Condens. Mat., 10 (1998) 7501-7510.
[74] M. Pollet, M. Daturi, S. Marinel, J. Eur. Ceram. Soc., 24 (2004) 1805-1809.
[75] P. McMillan, N.Ross, Phys. Chem. Miner., 16 (1988) 21-28.
[76] C.H. Perry, D.J. MacCarthy, G. Ruprecht, Phys. Rev., 138A (1965) 1537-1538.
[77] M. Tarrida, H. Larguem, M. Madon, Phys. Chem. Minerals, 36 (2009) 403-413.
[78] R. Borja-Urbya, L.A. Diaz-Torres, P. Salas, M. Vega-Gonzalez, C. Angeles-Chavez, Mat. Sci. Eng. B, 174 (2010) 169–173.
[79] Y.V.B.d. Santana, C.W. Raubach, M.M. Ferrer, F.L. Porta, J.R. Sambrano, V.M. Longo, E.R. Leite, E. Longo, J. Appl. Phys., 110 (2011) 123507.
[80] J.-L. Brédas, J.E. Norton, J. Cornil, V. Coropceanu, Acc. Chem. Res., 42 (2009) 1691-1699.
[81] B.M. Savoie, N.E. Jackson, T.J. Marks, M.A. Ratner, Phys. Chem. Chem. Phys., 15 (2013) 4538-4547.
[82] J. Kim, K. Hong, S.-Y. Hwang, S. Ryu, S. Choi, W.Y. Kim, Physical Chemistry Chemical Physics, 19 (2017) 10177-10186.